Fabrication of Ultra-Low Absorption Thin Films via Ion Beam Assisted Electron Beam Evaporation

Ruichen Song[1,2], Jiaqi Hu[2], Yunqi Peng[2], Yingao Xiao[2], Yuxiang Wang[2], Kongxu Zhu[2],Yuheng Jiang[2], Xusheng Xia[1,2], and Zhilin Xia[1,2]

[1] *Wuhan University of Technology, State key laboratory of advanced glass materials, Wuhan, China*

[2] *Wuhan University of Technology, Material Science and Engineering, Wuhan, China*

Correspondence to: Xusheng Xia. *Wuhan University of Technology, Material Science and Engineering, Wuhan, China.* Email:xsxia@whut.edu.cn.
Zhilin Xia. *Wuhan University of Technology, Material Science and Engineering, Wuhan, China.* Email:xiazhilin@whut.edu.cn.

Abstract High-power laser systems require thin films with extremely low absorption. Ultra-low absorption films are often fabricated via ion beam sputtering, which is costly and slow. This study analyzes the impact of doping titanium and annealing on the absorption characteristics of thin films, focusing on composition and structure. The results indicate that the primary factor influencing absorption is composition. By suppressing the presence of electrons or holes that do not form stable chemical bonds can significantly reduce absorption; For amorphous thin films, the structural influence on absorption is relatively minor. Thus, composition control is crucial for fabricating ultra-low absorption films, while the deposition method is secondary. Ion beam assisted electron beam evaporation, which is relatively seldom used for fabricating low-absorption films, was employed to produce high-reflectivity films. After annealing, the

absorption at 1064 nm reached 1.70 ppm. This method offers a cost-effective and rapid approach for fabricating ultra-low absorption films.

Key words: thin films, Ti doped Ta_2O_5, electronic structure, annealing treatment

I. INTRODUCTION

Optical films are commonly used for core components of high-precision, high-power laser instruments, such as gravitational wave interferometers, laser gyroscopes, laser inertial confinement fusion, laser communication devices, and laser ranging systems[1-6]. When high-energy laser acts on optical film, the film absorbs laser energy and causes temperature rise, resulting in deformation and a decrease in the performance of the optical system[7]. Therefore, to control the temperature rise of optical components during the operation of high-power laser systems and consequently improve beam quality and power density, it is essential to enhance the ability of thin film materials to suppress optical absorption.

Tantalum pentoxide(Ta_2O_5) has high transparency from near-ultraviolet to infrared bands, making it a commonly used high-refractive-index material in laser thin films[8]. Ta_2O_5 exhibits common challenges associated with metal oxides, particularly the difficulty in avoiding oxygen vacancies, which makes it difficult to reduce the absorption of the film[9]. Currently, doping and annealing are effective methods for suppressing thin film absorption. Annealing, by promoting extended relaxation, aids in stress release and the reduction of defects within the thin film structure[10,11]. Chen et al. prepared Ta_2O_5 film using a double-ion beam sputtering deposition system[12]. The absorption of the film decreased after heat treatment. Under the process conditions of 35 sccm of ionized oxygen and 40 sccm of oxygen flow, the film exhibited a low absorption of 1.2 ppm after annealing at 400℃. However, it is generally challenging to

2

completely eliminate defects in the film using annealing alone[13]. Doping is widely recognized as an effective method for reducing thin film absorption. Elements such as Ti, Zr, W, Co, Hf, and Si can be introduced as dopants during the deposition process, modifying the film's structure and absorption properties[14-16]. Harry et al. prepared Ta_2O_5 films with different concentrations of doped TiO_2 by ion beam sputtering and found that doping reduced the internal loss of the coating and the minimum absorption of the film could reach 0.9 ± 0.1 ppm, which is close to meeting the light absorption requirements of the second-generation gravitational wave detectors[17,18]. Doping will affect the optical absorption properties of the film, but there is currently no clear explanation for its influence rules and mechanisms.

The primary deposition techniques used for optical thin films include ion beam sputtering, reactive magnetron sputtering, electron beam evaporation, and atomic layer deposition[19-23]. Ion beam sputtering is currently the primary method for fabricating ultra-low absorption films. This technique produces samples with smooth surfaces and dense structures[12]. However, it is associated with high equipment costs, slow deposition rates, and high film stress[15]. In contrast, electron beam evaporation offers a more cost-effective solution with faster deposition rates, but it typically results in films that are more porous and have rougher surfaces[16]. As a result, electron beam evaporation is seldom used for the fabrication of ultra-low absorption films. In this study, Ti:Ta_2O_5 thin films were investigated through both experimental and simulation methods. Experimentally, ion beam-assisted electron-beam co-evaporation, was used to prepare Ti doped Ta_2O_5 monolayer and multilayer films, the obtained films were annealed at 500℃. The optical properties, microstructure, vibrational modes, and composition of the films were investigated. Theoretically, an amorphous Ta_2O_5 model was established using molecular dynamics, and the interactions between oxygen vacancies and titanium substituting for

3

tantalum were simulated. The electronic structure and optical properties of the model were then investigated using density functional theory. This demonstrates that electron beam evaporation can be used to fabricate ultra-low absorption films, offering a rapid and low-cost method.

II. Results

2.1 Optical constants and absorption

Ta_2O_5 films with different Ti doping levels were prepared using ion-assisted electron beam evaporation and all films were annealed at 500°C. The sample ID and the expected mass percentage of TiO_2 are shown in Table 1.

Table 1. Sample ID and expected mass ratios of TiO_2

Sample ID	Expected TiO$_2$ content
A	0
B	5%
C	10%
D	15%
E	20%
F	100%

Figure. 1(a) shows the transmittance spectra of the film at 200-1200nm under varying doping concentrations. The impurity of Ti significantly alters the ultraviolet cutoff edge of the film. As the amount of Ti doping increases, the cutoff edge gradually moves from sample A to F. Figure. 1(b) contains the refractive index(n) of all samples before and after heat treatment. Due to the higher refractive index of TiO_2 compared to Ta_2O_5, the refractive index of samples A through F increases with the Ti content. Furthermore, there are notable differences in the refractive index of the samples pre- and post-heat treatment. For sample F, which will be

4

discussed in Section 2.2, it is the only coating that undergoes a transition from an amorphous to a crystalline structure after heat treatment. The crystallization results in a higher density and a more ordered structure, leading to an increase in refractive index. In contrast, the other samples (A–E) remain amorphous, with a slight decrease in refractive index after annealing. This observation can be explained by the relationship between refractive index and packing density, suggesting that annealing reduces the film's packing density. These findings are consistent with the typically reported correlation between optical constants and annealing temperature[11].
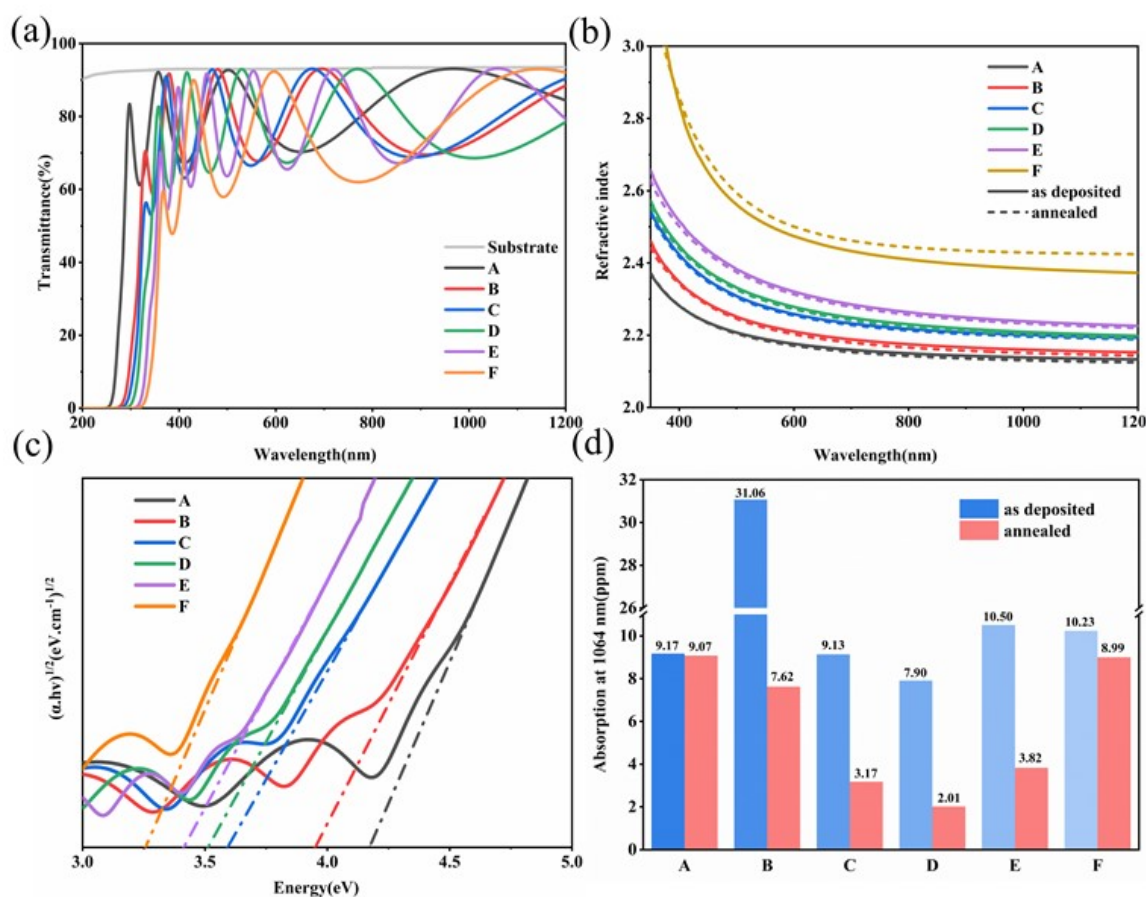
Figure 1. Optical properties of the films: (a) transmittance; (b) refractive index n; (c) band gap of unannealed samples; (d) absorption.

The optical band gap of the coating is estimated by the Tauc equation[16]. Figure. 1(c) shows the band gap of the unannealed samples, with sample A having a band gap of 4.169 eV,

and sample F having a band gap of 3.246 eV. The band gaps of the other doped samples decrease systematically with increasing doping concentration. According to Table S1 in the supplementary literature, the band gaps of all coatings exhibit a slight increase after annealing. Thermal treatment in air may induce relaxation in the film, potentially adjusting its composition and reducing defect density, which could further lead to an increase in the bandgap. This will be further explained in the components analysis and simulation part at section 2.4.

Figure. 1(d) shows the absorption of the film at 1064 nm. The value of unannealed films is represented in blue, while that of the annealed films is shown in red. For every identical sample, the red bar graph values are consistently lower than those of the blue bar graph, indicating that annealing effectively reduces the film's absorption. For undoped samples A and F, the absorption decreased from 9.17 ppm to 9.07 ppm and from 10.23 ppm to 8.99 ppm after annealing, respectively. This suggests that the annealing process can only partially reduce the absorption of pure Ta_2O_5 and TiO_2.

For doped, as-deposited films(B-E), except for sample D, exhibit absorption values that are almost equal to or exceed that of pure Ta_2O_5(A), particularly sample B (5%) shows an absorption of 31.06 ppm. This phenomenon may be attributed to the disorder among atoms within the microstructure of the mixed material, potentially caused by lattice distortion due to the addition of Ti, which increases defects in the film and consequently enhances absorption[16] For the annealed samples, absorption initially decreases and then increases with rising doping concentrations, suggesting that this behavior may be related to the material composition, with a detailed discussion provided in the section 2.3 on the formation energy and composition. Among these samples, the one with a designed doping concentration of 15%, sample D, exhibits the lowest absorption after annealing, at 2.01 ppm.

6

2.2 Structural characterization

Figure. 2 shows the XRD images of samples A(pure Ta_2O_5) and F(pure TiO_2) before and after heat treatment at 500°C. For sample A, there is minimal difference in the curves before and after annealing, with both curves appearing smooth and lacking distinct peaks, indicating an amorphous structure. In contrast, sample F shows a notable difference before and after annealing. Sample F before heat treatment is amorphous, and annealing causes the film to transform from amorphous to crystalline. The XRD spectrum shows obvious characteristic peaks of the anatase phase[24]. Typically, amorphous Ta_2O_5 begins to exhibit a hexagonal phase at temperatures above 650°C[11], whereas TiO_2 generally starts forming anatase crystals above 400°C. Thus, annealing at 500°C induces crystallization in the sample F but has negligible impact on the structure of the sample A. To further investigate the structural changes induced by doping and annealing, Raman spectroscopy was employed for additional analysis and characterization.
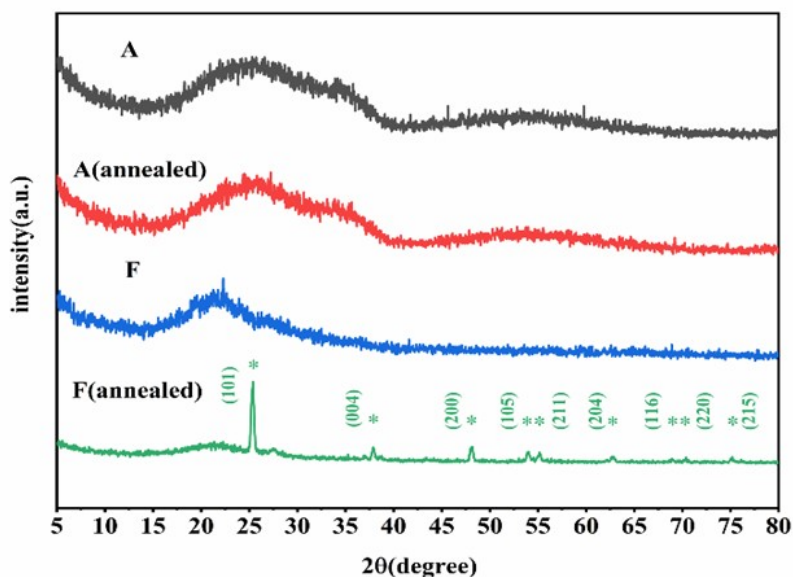

Figure 2. X-ray diffraction patterns of sample A (Ta_2O_5) and sample F (TiO_2) before and after annealing.

All samples were subjected to Raman spectroscopy analysis both before and after annealing process. To improve the analysis of peak positions, the data were smoothed using

7

techniques similar to those reported in previous studies[15]. The spectra, shown in Figure 3(a), as the film is transparent at 532nm, the test spectrum will contain information about the fused quartz. By comparing the spectrum with that of the background fused silica, the spectral bands around $460cm^{-1}$, $605cm^{-1}$ and 800 cm^{-1} are attributed to the substrate rather than the film[25]. Specifically, the band at 460 cm^{-1} is associated with the Si-O-Si bond angle distribution (around 440 cm^{-1}) and 4-membered SiO_4 defect rings(around 490 cm^{-1}). The boundary between these two bands is not clearly defined, likely due to changes in the quartz surface ring structure caused by polishing and surface cleaning of the substrate. The band at 605 cm^{-1} is attributed to 3-membered SiO_4 defect rings, while the band at 800 cm^{-1} is assigned to Si-O stretching vibrations. For the F sample with pure TiO_2, the difference before and after annealing is as obvious as that in the XRD experiment. The bands at $240cm^{-1}$, $450cm^{-1}$, and $610cm^{-1}$ of the film before annealing exhibit the characteristics of rutile phase. Considering their broadening(higher than $30cm^{-1}$), it can be concluded that the unannealed F is amorphous, with a poorly crystalline rutile structure present[26]. After annealing, the characteristic bands at $144cm^{-1}$, $400cm^{-1}$, $520cm^{-1}$, and $642cm^{-1}$ indicate the formation of a distinct anatase structure in sample F[24]. Notably, the band at 144 cm^{-1} corresponds to the first Raman active mode (Eg) of anatase, associated with the symmetric stretching vibration of the O-Ti-O bond. And the band at 400 cm^{-1} is attributed to the symmetric bending vibration of the O-Ti-O bond. The higher peak intensity and narrower peak broadening indicate that it has a high crystallinity, which is consistent with the XRD test results.
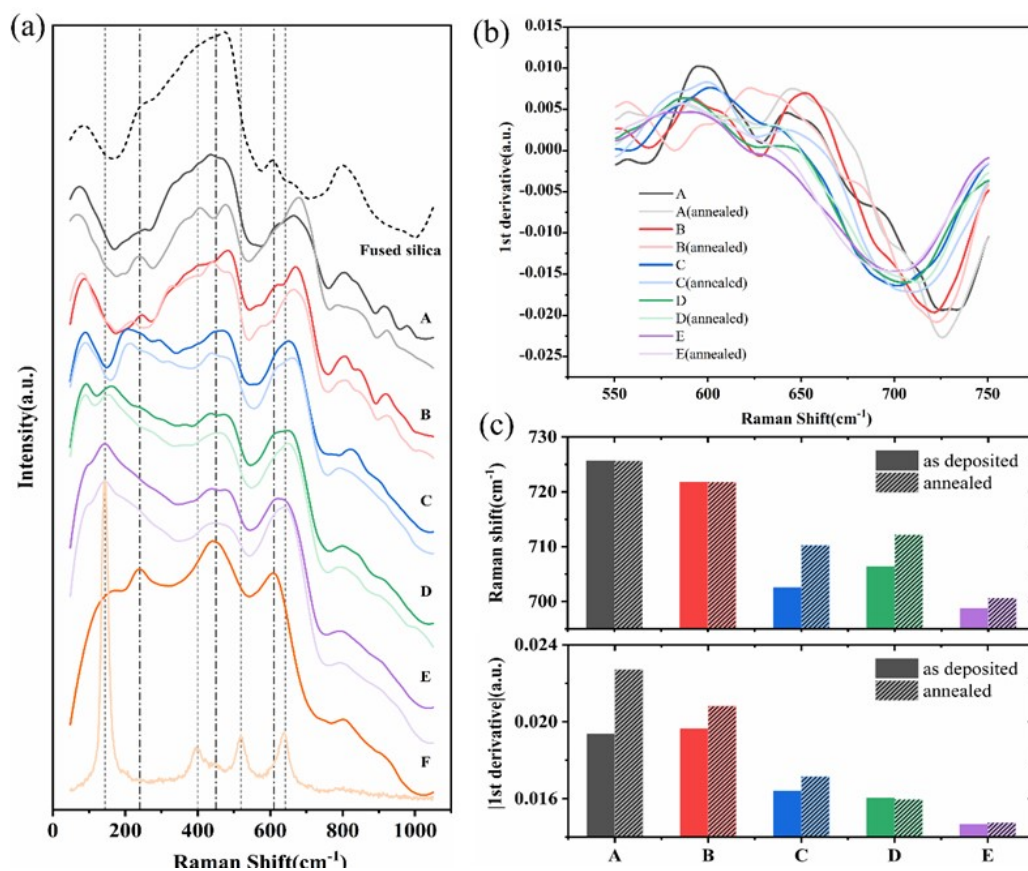
Figure 3. Raman analysis of the samples before and after annealing: (a) Raman spectra. The dark curve represents the unannealed sample, while the light curve corresponds to the annealed sample. Vertical lines indicate the diffraction peaks position of TiO$_2$ anatase (gray lines) and rutile (black lines) phases; (b) first derivative of the normalized Raman spectra in the 550-750 cm^{-1} region; (c) the horizontal coordinates (Raman shift) and the absolute values of the vertical coordinates corresponding to the extremum points of the normalized Raman spectra slopes for samples A to E.

Based on the peak widths of the spectral bands for samples A-E, it can be concluded that all of them exhibit an amorphous structure[27]. Since the primary component is Ta$_2$O$_5$, their spectral features are similar. After excluding the influence of the quartz glass substrate, the contributions of the thin films in the Raman spectra mainly appear in the ranges of 100-300 cm^{-1} and 550-750 cm^{-1}. For sample A(Ta$_2$O$_5$), the spectral features display typical characteristics of amorphous Ta$_2$O$_5$. After annealing, the mode around 240 cm^{-1} suggests that some crystallization has

9

occurred within the amorphous structure[27,28]. The modes in the 100-300 cm^{-1} range primarily arise from the bending vibrations of the O-Ta-O bonds in the TaO_6 octahedron[29]. This mode is highly sensitive to the Ti content. Even though Ta_2O_5 is the main material, the mode shifts to lower frequencies and its intensity increases with increasing Ti content. Sample B(5%), with a low Ti content, retains the spectral characteristics of Ta_2O_5. In the C (10%) sample, the mode at around 200 cm^{-1} cannot be independently assigned to Ta_2O_5 or TiO_2, suggesting that coupling between the O-Ta-O and O-Ti-O vibrations has occurred. For samples D (15%) and E (20%), the corresponding modes appear at 144 cm^{-1} and 130 cm^{-1}, respectively. These modes are closer to those observed in annealed sample F (TiO_2), indicating similarities to the rutile phase. The spectral bands in the 550-750 cm^{-1} range are attributed to the stretching vibrations of Ta-O bonds in TaO_6[28]. The variation in this region with Ti content is relatively less pronounced. Since sample F (pure TiO_2) exhibits a similar mode in the 600-650 cm^{-1} range before and after annealing, it can be inferred that the growth of the mode around 620 cm^{-1} in the Ti-doped Ta_2O_5 samples is due to the increased Ti content.

We aim to derive information about the film relaxation state from the peak broadening, which reflects the degree of ordering within the film. Roorda et al. reported a correlation between structural relaxation and the linewidth of Raman peaks, where a reduction in bond angle distribution leads to the sharpening of Raman peaks[30]. In this study, the main Raman contribution regions are between 100-300 cm^{-1} and 550-750 cm^{-1}. The former region shows larger shifts in peak positions with doping, and is interfered with by the substrate peak at around 70 cm^{-1}. Therefore, we focus on the latter region to assess the relaxation state of the films. Abernathy et al. demonstrated that the absolute value of the maximum slope can reflect the linewidth of Raman peaks composed of Lorentzian or Gaussian functions[15]. A larger slope

corresponds to a narrower peak, indicating better relaxation. We adopted a similar method by normalizing the 550-750 cm^{-1} range (Figure S1) and taking the first derivative, as shown in Figure 3(b). To provide a clearer visual representation, the changes in the coordinates of the slope minima for samples A to E before and after annealing are illustrated in Figure 3(c). The upper panel shows the changes in the horizontal coordinates (Raman shift) corresponding to the extremum points before and after annealing. For samples with TiO$_2$ content greater than or equal to 10% (C to E), the Raman shifts move toward higher frequencies after annealing, indicating that the incorporation of Ti modifies the internal microstructure of the films, resulting in additional changes during thermal treatment compared to samples A and B. The lower panel displays the changes in the absolute values of the vertical coordinates (|1st derivative|) corresponding to the extremum points before and after annealing. As previously mentioned, larger |1st derivative| correspond to narrower peak widths. For most samples, except D, the values increase after annealing, suggesting that the annealing process narrows the Raman peaks, leading to a more relaxed material. Furthermore, the gradual decrease in |1st derivative| with increasing Ti content implies a broadening of the peak width for this spectral band, indicating that the addition of Ti may, to some extent, reduce the structural relaxation.

2.3 Formation energy and composition

X-ray photoelectron spectroscopy (XPS) was utilized to observe the characteristic peaks of a series of doped films, with the peaks of the main elements being fitted for analysis. Figure. 4 and Figure. S2 present the XPS analysis of all samples before and after annealing, respectively, illustrating the chemical composition and electronic structure of the samples. According to existing research, the binding energy of Ta4f$_{7/2}$ for Ta^{5+} in Ta$_2$O$_5$ is typically in the range of 26.0-26.4eV[31]. Additionally, the binding energies for Ta-O and Ti-O bonds are approximately

530.5 eV, and the binding energy of Ti2p$_{3/2}$ is around 458.6 eV[16]. Table 2 summarizes the peak information for Ta, while the data for O and Ti are detailed in Table S2. The results indicate that the characteristic peaks of sample A and sample F with amorphous structures exhibit lower binding energies than these standard values. Notably, only sample F after annealing, which exhibits an anatase structure, shows a Ti2p$_{3/2}$ binding energy close to the standard value (458.63 eV). Therefore, the possible reason for the decrease in the binding energy mentioned above is that the amorphous structure of the film has a smaller binding energy than the standard crystal[32].

12
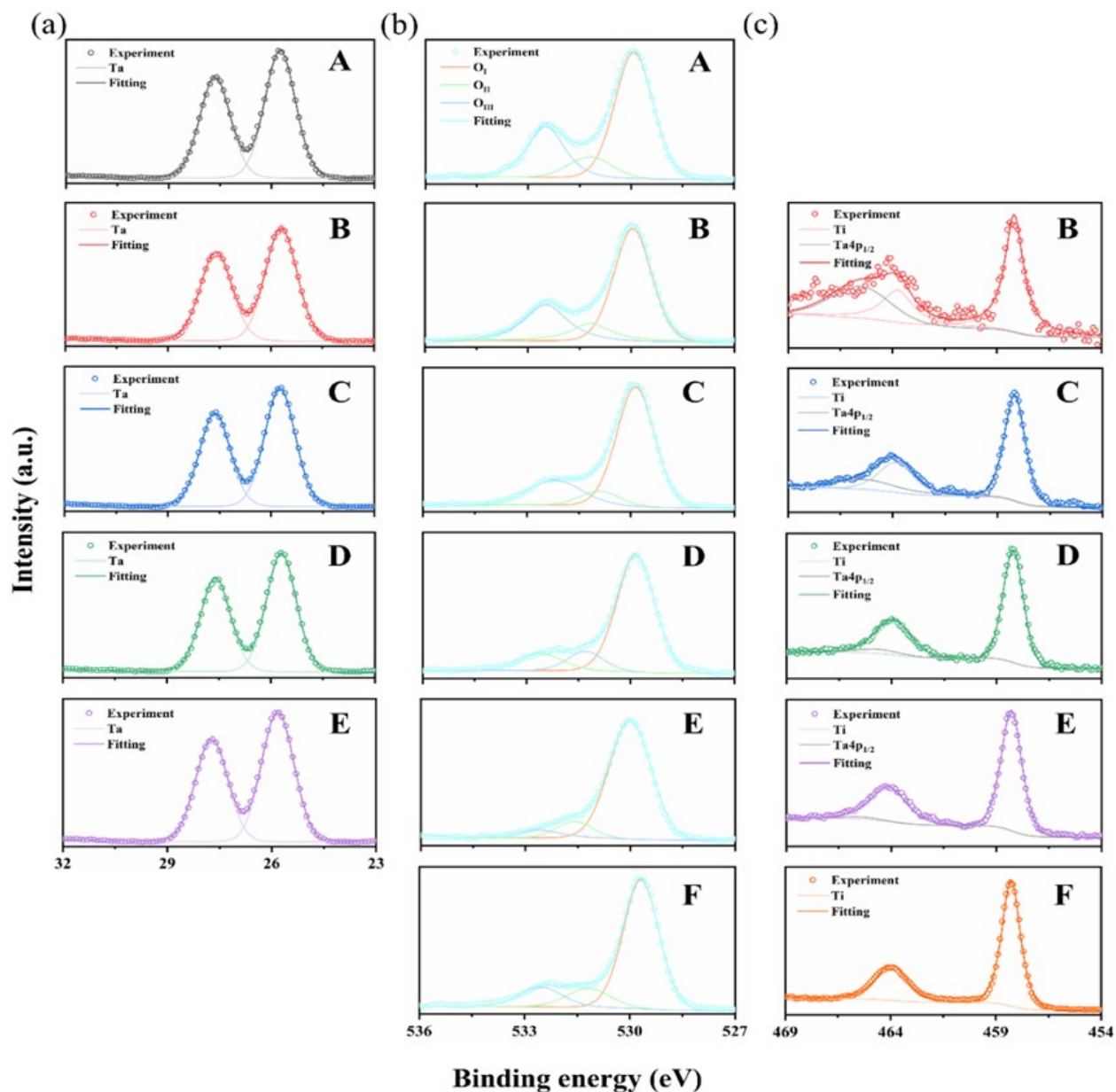
Figure 4. Typical XPS spectra of unannealed films: (a) Ta 4f; (b) O 1s (OI refers to lattice oxygen, OII corresponds to hydroxyl groups, and OIII represents surface-adsorbed oxygen.); (c) Ti 2p.

Figure. 4(a) illustrates that the typical Ta4f spectra in all Ta-containing coatings(A、B、C、D and E) display doublets (Ta4f$_{5/2}$ and Ta4f$_{7/2}$), corresponding to spin-orbit splitting, with a splitting energy of approximately 1.9 eV and an area ratio of about 3:4[31]. Table 2 shows that after heat treatment, the Ta4f$_{7/2}$ peak shifts to higher binding energies in all samples. For the as-

13

deposited Ti-doped samples, the position of the Ta4f$_{7/2}$ peak tends to decrease progressively with increasing Ti content. Existing reports have indicated that the direction of the Ta4f peak shift is related to the electronegativity of the doping elements, since the electronegativity of Ti is lower than that of Ta, the peak position shifts to lower energies[16]. The full width at half maximum (FWHM) of the characteristic peak can often reflect the concentration of different valence states in the material[33]. Except for sample C, the FWHM of the Ta4f$_{7/2}$ characteristic peak decreases in all Ta-containing samples after annealing compared to before annealing. This suggests that, in addition to Ta^{5+}, the samples also contain a small amount of Ta^{4+}, and that annealing can decrease the Ta^{4+} and increase the Ta^{5+} content. Before annealing, the FWHM of Ta4f$_{7/2}$ follows the order D < C = E < A < B, whereas after annealing, the order changes to D < E < A < C < B. Notably, the FWHM of samples D and E remains consistently smaller than that of sample A, indicating that higher concentrations of Ti doping can lead to a higher Ta^{5+} content in the films compared to pure Ta$_2$O$_5$ film.

Table 2. Fitting results of the Ta 4f7/2 peak for the films.

Sample	Binding energy(eV)		FWHM(eV)	
ID	As deposited	Annealed	As deposited	Annealed
A	25.68	25.75	1.10	1.09
B	25.70	25.76	1.16	1.14
C	25.66	25.74	1.09	1.11
D	25.66	25.79	1.05	1.01
E	25.64	25.83	1.09	1.06
F	--	--	--	--

Figure. 4(b) presents a typical XPS spectrum of O1s in the films. The OI peak is considered to correspond to lattice oxygen within the oxide, while the OII and OIII peaks are

14

generally attributed to oxygen in surface contaminants such as hydroxyl groups, adsorbed water, and carbonates[34]. Table S2 also provides the specific peak positions of O (lattice oxygen). For most samples, thermal treatment leads to an increase in the binding energy of lattice oxygen. In B, C, D, and E, the binding energy of O before heat treatment decreases progressively with increasing doping concentration. This change is attributed to the introduction of Ti doping, which creates holes and captures some electrons, thereby reducing the electron density of O and leading to a decrease in binding energy[35].

In all Ti-containing coatings(B、C、D、E and F), the Ti2p peaks can be fitted into two sub-peaks: $Ti2p_{1/2}$ and $Ti2p_{3/2}$. The splitting energy between these sub-peaks is approximately 5.8 eV, with an area ratio of about 1:2[16]. Figure. 4(c) shows the presence of the $Ta4p_{1/2}$ peak at the position of the Ti2p characteristic peak. Therefore, during peak fitting of all Ti-doped samples, the $Ta4p_{1/2}$ peak is identified and marked. As the Ti doping level increases, the relative intensity of the $Ta4p_{1/2}$ peak decreases, which is consistent with the observed trend in the expected Ta/Ti ratio.

Table 3. Elemental composition of the films and the calculated mass ratio of TiO_2.

Sample	XPS(Ta : Ti : O)		Measured TiO_2 content	
ID	As deposited	Annealed	As deposited	Annealed
A	32.89 : 0 : 67.11	31.71 : 0 : 68.29	0%	0%
B	29.01 : 5.51 : 65.47	27.63 : 5.25 : 67.12	6.425%	6.426%
C	23.71 : 8.75 : 67.55	22.94 : 8.48 : 68.58	11.770%	11.787%
D	19.62 : 11.77 : 68.61	18.93 : 11.31 : 69.76	17.820%	17.761%
E	17.62 : 11.52 : 70.86	17.99 : 11.77 : 70.25	19.116%	19.126%
F	0 : 31.98 : 68.02	0 : 32.79 : 67.21	100%	100%

The elemental composition of each coating before and after annealing was determined by XPS, and the resulting elemental and mass ratios are presented in Table 3. In this table, "XPS (Ta: Ti: O)" represents the elemental ratios obtained through peak fitting of the XPS spectra, while "Measured TiO_2 content" represents the percentage of TiO_2 in the total mass, derived from the elemental ratios. This value can be used for comparison with the data presented in Table 1. Although these measured ratios differ slightly from the expected mass ratios of the coatings, the variations among different doping levels are relatively pronounced. The slight changes in the relative content of Ta and Ti before and after annealing may be attributed to differences in the test locations, and these variations are within the acceptable range.
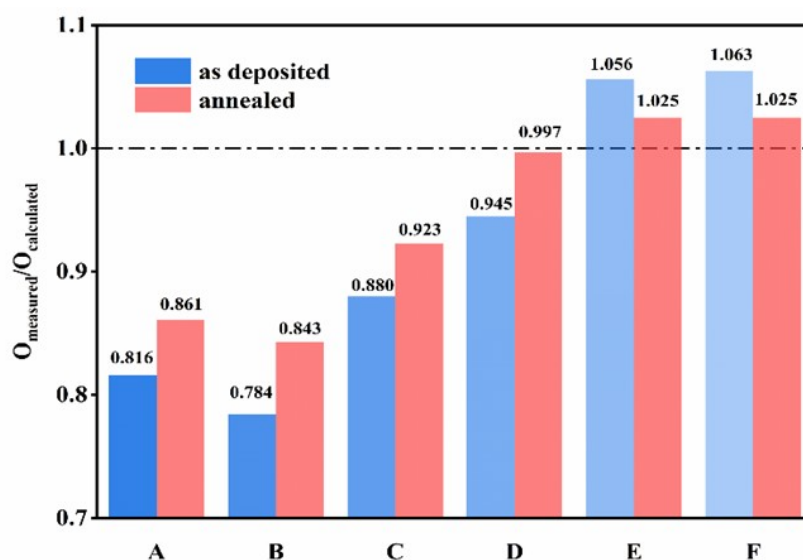
Figure 5. The ratio of $O_{measured}$ (measured Oxygen content) to $O_{calculated}$ (calculated stoichiometric Oxygen content) in the films.

Figure. 5 illustrates the comparison of oxygen content in all samples before and after annealing. Here, $O_{measured}$ represents the actual oxygen content measured experimentally, whereas $O_{calculated}$ refers to the oxygen content calculated based on the complete oxidation of Ta and Ti present in the tested films. The closer the ratio of $O_{measured}/O_{calculated}$ is to 1.0, the closer the actual oxygen content of the coating is to the standard stoichiometric ratio. The experimental

16

results indicate that the $O_{measured}/O_{calculated}$ ratio for Ta-containing samples is less than 1.0, suggesting an oxygen deficiency. In contrast, for sample F(TiO$_2$), this ratio is greater than 1.0, indicating an excess of oxygen, similar to the situation of oxygen excess in TiO$_2$ reported in the literature[36]. The ratio of all coatings approaches 1.0 after annealing, suggesting that annealing is an effective method for achieving an ideal stoichiometric ratio. However, for samples A and F, the ratios post-annealing only reach 0.861 and 1.025 respectively. To get closer to the standard stoichiometric ratio, doping is needed. The annealed films exhibit a relatively distinct pattern. For sample D, the $O_{measured}/O_{calculated}$ ratio is 0.997, which is the closest to 1.0. When the Ti content is below this doping level, the film exhibits an oxygen-deficient state, whereas a higher Ti content results in over-oxygenation.

This trend is consistent with the absorption of the films in Figure. 1(d). For sample A, the ratio of $O_{measured}/O_{calculated}$ increases from 0.816 to 0.861, with absorption values of 9.17 ppm before annealing and 9.07 ppm after. This increase in the ratio corresponds to a decrease in absorption; however, since the ratio does not approach 1.0, the absorption value remains relatively high. Before annealing, the absorption of Sample B is as high as 31.06 ppm. The stoichiometric ratio of the film is Ta:Ti:O = 29.01:5.51:65.47, with the ratio $O_{measured}/O_{calculated}$ = 0.784, indicating that the film is in an oxygen-deficient state, which represents the largest deviation from the ideal stoichiometry. After annealing, the ratio increased to 0.843, indicating a rise in oxygen content, while the absorption decreased to 7.62 ppm. And the annealed Sample D exhibits the lowest absorption of 2.01 ppm. At this doping level, the film's $O_{measured}/O_{calculated}$ ratio is 0.997, indicating a composition that is closest to the stoichiometric ratio expected for fully oxidized Ta and Ti. For sample E, the film exhibits an $O_{measured}/O_{calculated}$ ratio of 1.056 before annealing, with an absorption of 10.50 ppm, indicating an over-oxidized state. After

17

annealing, the ratio decreases to 1.025, and absorption reduces to 3.82 ppm. This suggests that annealing can improve the oxygen deficiency and excess in the film, bringing its chemical composition closer to the ideal stoichiometric ratio, thereby achieving lower absorption values. In general, these observations are consistent with the trend that the closer the Ta and Ti in the film are to being fully oxidized, the lower the absorption.

Based on the above experimental results, we speculate that absorption is related to the chemical composition of the film. After annealing, absorption decreased to varying degrees, indicating that heat treatment in air atmosphere would make the film closer to the ideal stoichiometric ratio; for undoped films, annealing had limited effect on the reduction of absorption, indicating that it is difficult to achieve full oxidation of thin film materials with pure Ta_2O_5 and TiO_2 simply by heat treatment, and by doping with Ti, the composition of the coating after annealing can be closer to the standard stoichiometry, thereby further reducing the absorption; however, under fixed heat treatment conditions, there is an optimal range for TiO_2 content, and absorption will increase if it is lower or higher than this range. The following will explain the influence of components on the absorption of thin films through theoretical simulations.

2.4 Theoretical calculation and analysis of Ti doped Ta_2O_5

In order to explain the optimal range of Ti doping from a mechanistic perspective and why the absorption is lower within this range, Ti-doped amorphous Ta_2O_5 models were established. To ensure the validity of the initial model, we first plotted the pair distribution function (PDF) based on the amorphous Ta_2O_5 structure obtained from AIMD simulations, as shown in Figure. 6. The plot confirms that the structure is indeed amorphous, which is consistent with previous reports[37]. The first peak of the PDF for the Ta-O bond is observed at 1.93 Å, for

18

the O-O bond at 2.83 Å, and for the Ta-Ta bond at 3.76 Å. The peak values fall within the range reported in experimental studies: 1.92-1.99 Å for the Ta-O bond and 3.14-3.88 Å for the Ta-Ta bond[38].

Based on the experimental observations, we introduced two types of defects into the theoretical model. XPS analysis of sample A revealed the presence of oxygen vacancies in the Ta_2O_5 film, which we simulated by removing oxygen atoms. For the introduction of titanium, we chose to substitute Ti atoms for Ta atoms. During the dual-source co-evaporation process, Ti atoms occupy a fraction of the deposition sites originally intended for Ta atoms. Upon oxidation, Ti atoms bond with oxygen, replacing the regions where Ta-O polyhedra would have formed with Ti-O polyhedra. Considering that octahedral coordination of TaO_6 is predominant in amorphous Ta_2O_5[37], and the small voids in the structure lead to high defect formation energies for Ti atoms in interstitial sites, substitution sites are chosen. By removing one O atom from the amorphous Ta_2O_5 structure and replacing one, two, and three Ta atoms with an equivalent number of Ti atoms, we developed three doped models: $1V_O+1Ti_{Ta}$, $1V_O+2Ti_{Ta}$ and $1V_O+3Ti_{Ta}$. After structural relaxation, the lattice vector changes, as shown in Figure. S3, and there is no significant structural migration.
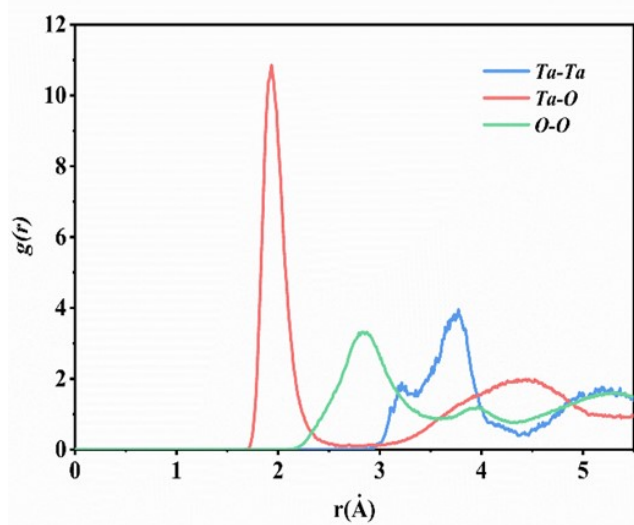
Figure 6. Pair distribution function of the simulated amorphous Ta_2O_5 model.

To further investigate the contribution of elemental composition to the impurity energy levels within the bandgap of the $Ti:Ta_2O_5$ model, the density functional theory (DFT) method was used to calculate the partial density of states (PDOS), with the zero-energy level set at the top of the valence band, as shown in Figure. 7. For the pure amorphous Ta_2O_5 model, the calculated bandgap is 4.43 eV, which is slightly higher than the previously reported experimental values of 3.8 eV to 4.3 eV[39]. As shown in Figure. 7(a), there is strong hybridization between the O 2p and Ta 5d orbitals in the valence band, resulting in a bandwidth of approximately 6.5 eV, which is consistent with previously reported theoretical calculations[9]. The top of the valence band is primarily contributed by the O 2p orbitals, while the bottom of the conduction band is mainly composed of contributions from the Ta 5d orbitals. In crystalline structures, the crystal field effect of the TaO_6 octahedra typically causes energy level splitting of the Ta 5d orbitals in the conduction band. However, due to the inherent disorder in the amorphous structure, the Ta 5d orbitals in the conduction band of this study's model do not split into the t_{2g}($3d_{xy}$、 $3d_{xz}$ 和 $3d_{yz}$) and e_g($3d_{x^2-y^2}$ 和 $3d_{z^2}$) orbitals as they do in crystalline structures[40].
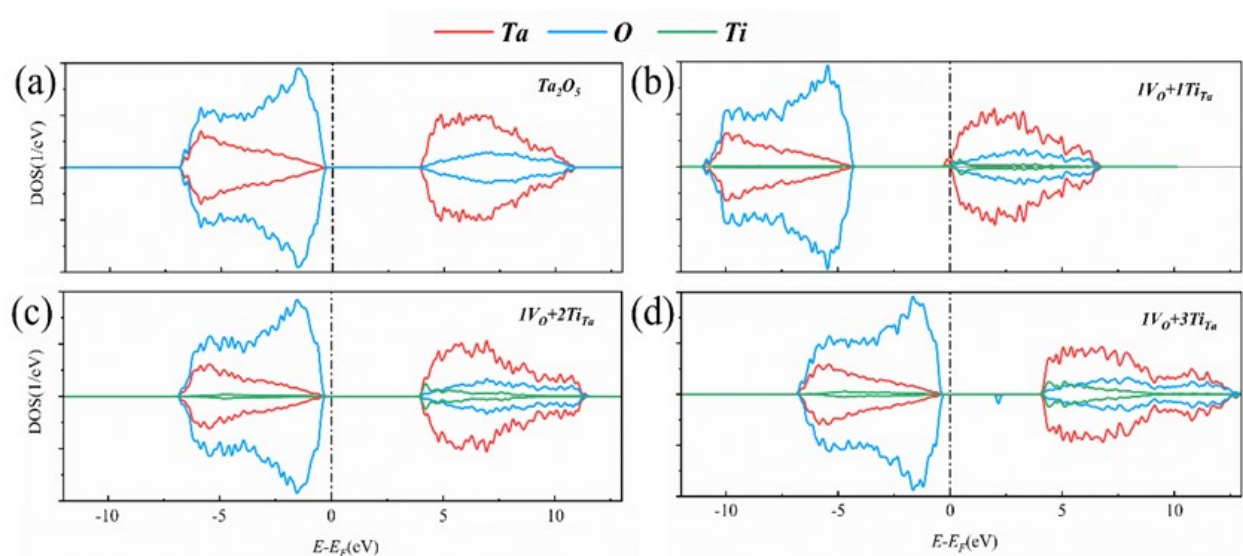
Figure 7. Theoretically calculated density of states: (a) Ta_2O_5; (b) $1V_O + 1Ti_{Ta}$; (c) $1V_O + 2Ti_{Ta}$; (d) $1V_O + 3Ti_{Ta}$. V_O represents an oxygen vacancy, which involves the removal of an Oxygen atom. Ti_{Ta} refers to the replacement of tantalum with titanium.

For the doping models, previous studies have reported that when an O vacancy is created, electrons that have not formed stable chemical bonds may interact with nearby Ta atoms to form weakly bound states such as dangling bonds, due to the Coulomb effect[9]. Since the energy associated with these states is higher than that of covalent bond formation, a donor energy level is introduced near the bottom of the conduction band above the valence band. Similarly, considering some cases of p-type doping[41], we hypothesize that when Ti atoms are substituted at Ta sites in the model, Ti provides fewer electrons to the surrounding environment compared to Ta, leading to the formation of holes on nearby oxygen atoms and the establishment of acceptor energy levels. When both types of doping are present, electrons from the donor energy levels preferentially occupy the acceptor energy levels. This phenomenon is known as "impurity compensation"[40].

For a structure containing one O vacancy and one Ti impurity, denoted as $1V_O+1Ti_{Ta}$, as shown in Figure. 7(b), the impurity energy level corresponds to the Ta 5d orbital, located 0.47 eV above the bottom of the conduction band. The PDOS is similar to those of previously reported oxygen vacancy defects, with the donor energy level just below the conduction band also associated with the Ta 5d orbital. From the perspective of impurity compensation, the presence of V_O is in excess, and the acceptor energy level introduced by Ti_{Ta} doping cannot fully accommodate all the donor charges from V_O. Therefore, this type of defect is similar to oxygen vacancy.

In the $1V_O+2Ti_{Ta}$ structure, Figure. 7(c) shows that the top of the valence band is primarily composed of O2p orbitals, while the bottom of the conduction band comprises

21

contributions from both Ta 5d and Ti 3d orbitals. The electrons from the donor energy level generated by the oxygen vacancy are exactly compensated by the acceptor energy levels introduced by the Ti_{Ta} dopants. As a result, all electrons participate in the formation of stable chemical bonds, leaving no unoccupied states in the bandgap. Figure. 8 illustrates the differential charge distribution for the $1V_O+2Ti_{Ta}$ structure, with Ta atoms represented in golden, O atoms in red, and Ti atoms in blue. The blue electron cloud indicates regions of electron loss, while the yellow regions denote areas of electron gain. The differential charge analysis reveals that electron loss primarily occurs at Ta atoms adjacent to the O vacancy, while electron gain is predominantly concentrated on the two Ti atoms and the nearby O atoms. The coexistence of V_O and Ti_{Ta} results in electron transfer from Ta to Ti within the system. As previously mentioned, the positively charged centers formed by Ta at oxygen vacancies interact with electrons to create dangling bonds, which are weaker than stable chemical bonds. When Ti replaces Ta, it generates holes in the surrounding structure. These holes attract nearby electrons, particularly those forming weak bonds with Ta, leading to observable electron loss at Ta sites and electron gain at Ti sites. The bandgap of the $1V_O+2Ti_{Ta}$ structure is calculated to be 4.40 eV, which is slightly smaller than that of the pure Ta_2O_5 model.

22
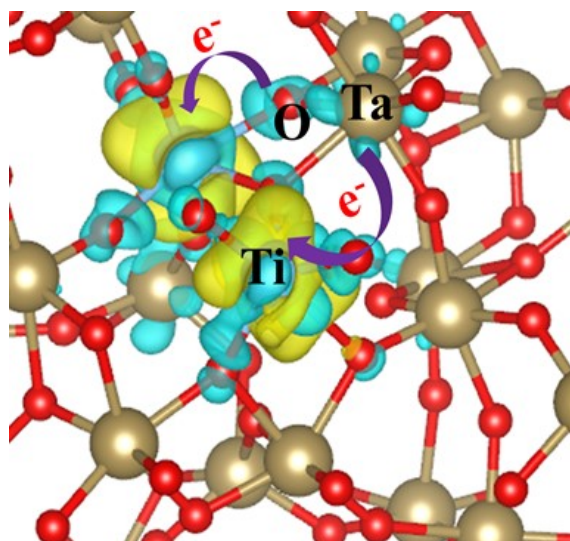
Figure 8. Differential charge distribution around Ti atoms in the $1V_O+2Ti_{Ta}$ model. The golden sphere represents a tantalum atom, the blue sphere represents a titanium atom, and the red sphere represents an oxygen atom. The blue electron cloud indicates a loss of electrons, while the yellow cloud represents a gain of electrons.

When a $1V_O+3Ti_{Ta}$ configuration is introduced into the system, Figure. 7(d) illustrates the formation of an acceptor energy level just above the valence band, with the acceptor state being predominantly composed of O 2p orbitals, located 1.79 eV above the valence band maximum. In this model, the Ti_{Ta} concentration is excessive, and the electrons from the donor energy level associated with the O vacancy do not fully compensate for the holes generated by the Ti atom. As a result, the system exhibits characteristics typical of acceptor doping.
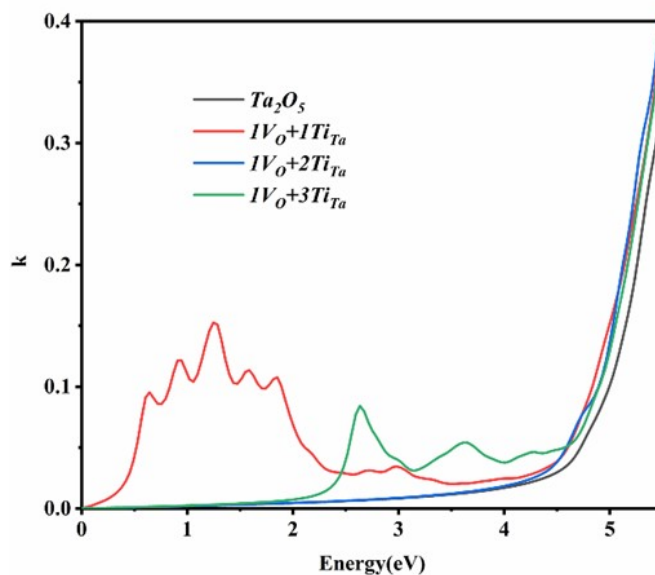
Figure 9. Theoretically calculated extinction coefficient k.

The impurity energy levels within the energy band significantly influence the photoelectric properties of the system. Under the influence of external light and heat, electrons in the donor energy level can be readily excited into the conduction band, and electrons in the valence band can similarly be excited into the unoccupied acceptor energy levels. These processes result in increased absorption by the material, leading to an undesirable increase in

23

absorption. The perspective can also be confirmed by the calculated extinction coefficient. Figure. 9 presents the extinction coefficient curves of the four models as a function of energy. The absorption region for the $1V_O+1Ti_{Ta}$ is observed between 1eV and 3eV, while the $1V_O+3Ti_{Ta}$ shows absorption above approximately 2 eV. In contrast, the extinction curves for Ta_2O_5 and $1V_O+2Ti_{Ta}$ exhibit no peaks within the 0-4 eV range.

Thus, to obtain low absorption materials, the compositions corresponding to Ta_2O_5 and $1V_O+2Ti_{Ta}$ are relatively ideal. However, producing a Ta_2O_5 coating without oxygen vacancies through conventional heat treatment processes poses significant challenges. We aim to achieve a coating with the target composition of $1V_O+2Ti_{Ta}$ through controlled doping and annealing. Based on the experimental results, it can be concluded that $1V_O+1Ti_{Ta}$ corresponds to samples B and C, $1V_O+2Ti_{Ta}$ corresponds to sample D, and $1V_O+3Ti_{Ta}$ corresponds to sample E. This also explains that as the doping concentration increases, the absorption of annealed samples first decreases and then increases. Outside the appropriate range, an excess or deficiency of Ti introduces extra charges into the film, leading to increased absorption.

In summary, both experimental and theoretical evidence demonstrate that composition is the primary factor influencing thin film absorption, while the deposition method typically affects the film's density and structure. Therefore, we conclude that, with proper control of composition, low-absorption films can still be fabricated using ion beam assisted electron beam evaporation, even without employing ion beam sputtering.

2.5 Preparation of high- reflectivity film

Based on the process of sample D, which exhibited the lowest absorption, we used it as the high-refractive-index layer (H) to fabricate high-reflectivity layer. SiO_2, a material with very low absorption, was used for the low-refractive-index layer (L), and the multilayer structure

followed the design Substrate / (HL) [17] /Air, with quarter-wave(QW) optical thicknesses at 1064nm. The multilayer film underwent the same heat treatment as the single-layer films. The transmission curve of the high-reflectivity film is shown in Figure. 10, demonstrating high reflectivity across the 950-1130 nm wavelength range. The absorption at 1064 nm was measured before and after annealing, showing a reduction from 66.39 ppm to 1.70 ppm after heat treatment. Most ultra-low absorption thin films are currently fabricated using ion beam sputtering(IBS). In this experiment, it is demonstrated that by combining compositional control with annealing processes, ultra-low absorption thin films can be achieved through ion beam-assisted electron beam evaporation.
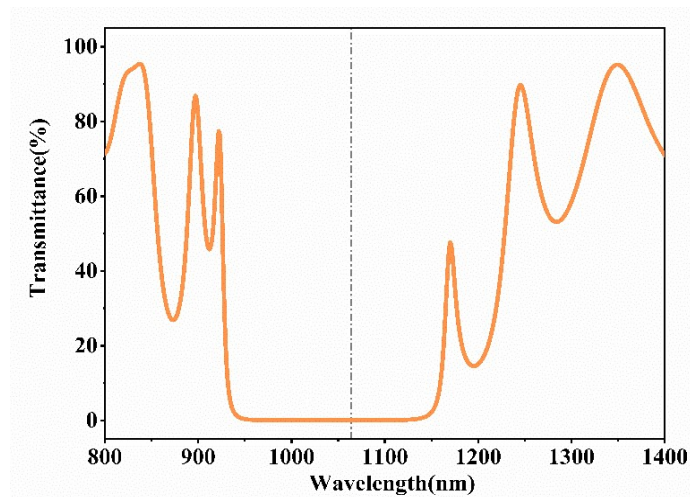
Figure 10. Measurement of transmittance spectrum of high- reflectivity film.

III. DISCUSSION

Single-layer and multilayer Ta_2O_5 films with varying Ti concentrations were fabricated using ion beam assisted electron beam evaporation and annealed at 500°C. The experimental results show that all films are amorphous before heat treatment. Compared to structural factors, the composition appears to have a more significant impact on absorption. Amorphous films with compositions closer to the fully oxidized states of Ta and Ti exhibit lower absorption. From a

25

structural perspective, TiO_2 significantly alters the Raman response of the films and appears to increase structural disorder. In contrast, annealing tends to relax the structure of films. From a compositional standpoint, both doping and annealing contribute to bringing the films closer to the ideal stoichiometric ratio. However, relying solely on one of them has limitations. A combination of doping and annealing is required to achieve the optimal condition, corresponding to ultra-low absorption. Theoretical calculations reveal the charge transfer associated with the introduction of Ti, which "neutralizes" oxygen vacancies, and explain that there is an optimal concentration range for Ti. When the actual content of TiO_2 is around 17.8%, the absorption of the single-layer film at 1064nm can be reduced to 2.01ppm after annealing, and the absorption of the high-reflectivity film prepared using this process reached 1.70 ppm after annealing. This implies that, with the correct composition, low-absorption films can be fabricated even without the need for high-cost deposition methods such as ion beam sputtering. This study provides theoretical and technical insights for the lower-cost, faster fabrication of ultra-low absorption films.

IV. METHODOLOGY

4.1 Experimental methods

A series of thin films were experimentally deposited on fused silica substrates (Φ25.4 mm $\times$ 2.5 mm) using an ion beam assisted electron beam co-evaporation process under O_2/Ar atmospheric conditions. The substrates were subjected to super-polishing, followed by ultrasonic cleaning and thorough rinsing with deionized water(18.2MΩ·cm). The baseline vacuum level was maintained at 1.0×10^{-4} Pa, and the deposition temperature was set to 250°C. The materials used for the film deposition were Ta with a purity of 99.99% and Ti_3O_5 particles, with a particle size ranging from 1 to 3 mm and a purity of 99.99%. During the evaporation process, the

substrates were positioned on the sample holder above the electron beam evaporation system. The oxygen ion beam generated by the RF ion source bombards the surface of the film, enhancing the oxidation of the coating while simultaneously assisting in the deposition process, resulting in a denser film structure. The voltage applied to the auxiliary ion source is 1100 V, with a current of 1000 mA.

Pre-experiments were conducted prior to doping. Based on the relationship between the deposition rates of Ta_2O_5 and TiO_2 single layers and beam current, single-layer films with different doping ratios were prepared by pre-set Ta and Ti deposition beam current according to the designed doping film composition. The actual doping composition of these single layers was characterized using XPS, which allowed for the determination of the beam currents for each component during the preparation of layers with different doping ratios. Subsequently, deposition time was controlled to fabricate doped single layers of varying thicknesses. The optical thickness of these doped layers was obtained through transmission spectral fitting, establishing a relationship between optical thickness and deposition time under the specified process parameters. Finally, during the deposition of multilayer films, the layer thickness was controlled by adjusting the deposition time. In the process of preparing high-reflectivity films, the deposition rate for $Ti:Ta_2O_5$ was 2Å/s, and that for SiO_2 was 6Å/s. Throughout the entire process, the crystal monitor was only employed as an auxiliary tool during the deposition of pure TiO_2 and Ta_2O_5 single layers. The deposited samples underwent an annealing process, with the temperature increased at a rate of 100°C/h from room temperature to 300°C, held at 300°C for 8 hours, then ramped up to 500°C at a rate of 50°C/h. After reaching 500°C, the temperature was maintained for 10 hours, followed by cooling to 350°C at 50°C/h. Finally, the samples were

allowed to cool naturally to room temperature. The entire heat treatment process was conducted in a muffle furnace.

The transmittance of the samples in the wavelength range of 200 to 2500 nm was measured using a Cary 5000 UV-Vis-NIR spectrophotometer, with a measurement accuracy of $\pm 0.06\%$. The refractive index (n) and optical band gap of the films were estimated using the transmittance spectra method and the Tauc equation, respectively[42,43]. The absorption of the samples in the 1064 nm was measured using laser induced deflection (LID) technology, with single-point testing performed using a continuous laser[44]. The structure of the coating was characterized using an Empyrean X-ray diffractometer (XRD), with measurements taken at a grazing incidence angle of 0.5°. Raman scattering was analyzed using a LabRAM Odyssey spectrometer with a 532 nm laser. The binding energies of Ta, O, and Ti in the films were determined by X-ray photoelectron spectroscopy (XPS) using a monochromatic Al Kα source (1486.6 eV) on a Thermo ESCALAB 250Xi instrument. Charge correction was applied using the C1s standard peak at 284.8 eV, and the obtained spectra were fitted using peak deconvolution techniques[45].

4.2 Computational methods

The simulation calculation of Ta_2O_5 and $Ti:Ta_2O_5$ was implemented based on DFT using the Vienna Ab initio Simulation Package software(VASP)[46]. Ta, O and Ti used the projector augmented wave (PAW) potentials Ta_pv, O and Ti_sv to treat the electron and ion interactions, and the spin polarization calculation was performed. Considering that real thin films are often disordered, we employed ab initio molecular dynamics (AIMD) to model the amorphous structure of the Ta_2O_5 lattice[27]. The calculation used the Perdew-Burke-Ernzerhof (PBE) generalized gradient approximation (GGA) to describe the exchange-correlation functional[47],

28

and the electronic structure iteration convergence threshold was set to 10^{-6} eV. The orthorhombic phase λ-Ta_2O_5 proposed by Lee et al. was used as the primitive cell[48], with lattice constants of a = 6.25Å, b = 7.40Å, and c = 7.66Å. A $2 \times 2 \times 2$ supercell containing 32 Ta atoms and 80 O atoms was created. According to the research of Christian Søndergaard Pedersen et al., we enlarged the lattice vector of the supercell by a factor of 1.06 to make it more consistent with the experimental value of the density of amorphous Ta_2O_5[49]. The supercell was subjected to a melt-and-quench procedure in the NVT ensemble using a Nose-Hoover thermostat: 10 ps equilibration at 4000 K, then quenched at 1000 K below the theoretical melting point, the cooling process lasted 20 ps and equilibration for 20 ps at 1000 K. The AIMD simulation used a low-precision setting with a cutoff energy of 200 eV, a $1\times1\times2$ k-points sampling, and a time step of 2 fs[50].

The ion positions and lattice vectors of the established Ta_2O_5 structure are structurally optimized by PBEsol functional, which provides better structural properties for the solid. The Brillouin zone was sampled with a $1\times1\times2$ k-points grid for structural relaxation[51]. The atomic force converges to within 0.02eV/Å, and the cutoff energy is increased to 520 eV. The average density of the final Ta_2O_5 is 7.606g/cm^3, which is within the experimental value (6.88-7.68 g/cm^3)[37]. The k-points sampling of the static self-consistent is increased to $2\times2\times4$. High-precision calculations of the obtained structures were performed using the Heyd-Scuseria-Ernzerhof (HSE06) hybrid functional to obtain accurate electronic structures[52]. Due to their high computational requirements, these calculations only used a $1\times1\times2$ k-points sampling. Different electron state densities can cause different dielectric responses.

The dielectric function $\varepsilon = \varepsilon_1(\omega) + i\varepsilon_2(\omega)$ is an important function for describing optical properties. The imaginary part $\varepsilon_2(\omega)$ is a collection of optical properties and can be described as formula (1)

29

$$\varepsilon_2(\omega) = \frac{2e^2\pi}{\Omega\varepsilon_0} \sum_{k,v,c} |\psi_k^c| \hat{u} \times r |\psi_k^v|^2 \delta(E_k^c - E_k^v - E) \quad (1)$$

Where Ω is the unit cell volume, v and c represent the valence band and conduction band respectively, k represents the k-point, ω is the incident light frequency, and $\hat{u}$ is the vector defining the polarization direction of the incident light field, which is considered to be an isotropic average value in the case of polycrystalline. The real part $\varepsilon_1(\omega)$ is obtained by the Kramers-Kronig relations[53]

$$\varepsilon_1(\omega) = 1 + \frac{2}{\pi} p \int_0^\infty \frac{\omega' \varepsilon_2(\omega')}{\omega'^2 - \omega^2} d\omega' \quad (2)$$

In the formula, p represents the principal value of the integral. The extinction coefficient $k(\omega)$ can be calculated using the following formula (3), based on the obtained $\varepsilon_1(\omega)$ and $\varepsilon_2(\omega)$[54].

$$k(\omega) = [\sqrt{\varepsilon_1^2(\omega) + \varepsilon_2^2(\omega)} - \varepsilon_1(\omega)]^{1/2}/\sqrt{2} \quad (3)$$

Acknowledgement

[1]. W. Zhang, T. Xian, W. Wang, and L. Zhan, "Advancement and expectations for mode-locked laser gyroscopes," J. Opt. Soc. Am. B-Opt. Phys. **39**(12), 3159-3168 (2022). DOI: https://doi.org/10.1364/JOSAB.460946

[2]. F. Meylahn, N. Knust, and B. Willke, "Stabilized laser system at 1550 nm wavelength for future gravitational-wave detectors," Phys. Rev. D. **105**(12), 122004 (2022). DOI: https://link.aps.org/doi/10.1103/PhysRevD.105.122004

[3]. V.Georgios, M. Giacomo, B. James, B. Robert, and G. Gianluca, "Detection of high-frequency gravitational waves using high-energy pulsed lasers," Class. Quantum Gravity. **40**(15), 155006 (2023). DOI:

https://dx.doi.org/10.1088/1361-6382/acd517

[4]. B. C. Nichol, R. Srinivas, D. P. Nadlinger, P. Drmota, D. Main, G. Araneda, C. J. Ballance, and D. M. Lucas, "An elementary quantum network of entangled optical atomic clocks," Nature. **609**(7928), 689-694 (2022). DOI:

https://doi.org/10.1038/s41586-022-05088-z.

[5]. X. Li, B. Zhang, M. Lin, and L. Qi, "Numerical analysis of thermal distortion of the mirror in space-to-ground laser communication links," Optoelectron. Lett. **1**(3), 209-212 (2005). DOI:

https://doi.org/10.1007/BF03033845

[6]. T. W. Murphy, E. G. Adelberger, J. B. R. Battat, C. D. Hoyle, N. H. Johnson, R. J. Mcmillan, E. L. Michelsen, C. W. Stubbs, and H. E. Swanson, "Laser ranging to the lost Lunokhod 1 reflector," Icarus. **211**(2), 1103-1108 (2011). DOI:

https://doi.org/10.1016/j.icarus.2010.11.010

[7]. D. Li, X. Niu, J. Xia, H. Jiao, X. Dun, J. Zhang, X. Cheng, and Z. Wang, "Research on the core factors affecting the temperature rise of dichroic mirrors in wavelength beam combination system under high-power CW laser," Opt. Commun. **552**, 130034 (2024). DOI:

https://doi.org/10.1016/j.optcom.2023.130034

[8]. J. Wen, M. Zhu, J. Sun, J. Li, and J. Shao, "Research progress on absorption loss control of laser coating," Acta Optical Sinica. **42**(7), 0700001 (2022). DOI:

https://doi.org/10.3788/AOS202242.0700001

[9]. Y. Guo, and J. Robertson, "Comparison of oxygen vacancy defects in crystalline and amorphous Ta_2O_5," Microelectron. Eng. **147**, 254-259 (2015). DOI:

https://doi.org/10.1016/j.mee.2015.04.065

[10]. W. Ren, G. D. Yang, A. L. Feng, R. X. Miao, J. B. Xia, and Y. G. Wang, "Annealing effects on the optical and electrochemical properties of tantalum pentoxide films," J. Adv. Ceram. **10**(4), 704-713 (2021). DOI:

https://doi.org/10.1007/s40145-021-0465-2

[11].   Q. Lv, M. Huang, S. Zhang, S. Deng, F. Gong, F. Wang, Y. Pan, G. Li, and Y. Jin, "Effects of Annealing on Residual Stress in Ta_2O_5 Films Deposited by Dual Ion Beam Sputtering," Coatings. **8**(4), 150 (2018). DOI: https://doi.org/10.3390/coatings8040150

[12].   C. Chen, Y. Wang, J. Feng, Z. Wang, Y. Chen, Y. Lu, Y. Zhang, D. Li, Y. Cui, and J. Shao, "Effect of ionic oxygen concentration on properties of SiO_2 and Ta_2O_5 monolayers deposited by ion beam sputtering," Opt. Mater. **136**, 113349 (2023). DOI: https://doi.org/10.1016/j.optmat.2022.113349

[13].   S. Sayah, B. Sassolas, J. Degallaix, L. Pinard, C. Michel, V. Sordini, and G. Cagnoli, "Point defects in IBS coating for very low loss mirrors," Appl. Optics. **60**(14), 4068-4073 (2021). DOI: https://doi.org/10.1364/ao.415462

[14].   K. M. A. Salam, H. Fukuda, and S. Nomura, "Reduction of defect states of tantalum oxide thin films with additive elements," Mater. Sci. Semicond. Process. **6**(5-6), 531-533 (2003). DOI: https://doi.org/10.1016/j.mssp.2003.04.001

[15].   M. Abernathy, A. Amato, A. Ananyeva, S. Angelova, B. Baloukas, R. Bassiri, G. Billingsley, R. Birney, G. Cagnoli, M. Canepa, M. Coulon, J. Degallaix, A. Di Michele, M. A. Fazio, M. M. Fejer, D. Forest, C. Gier, M. Granata, A. M. Gretarsson, E. M. Gretarsson, E. Gustafson, E. J. Hough, M. Irving, É. Lalande, C. Lévesque, A. W. Lussier, A. Markosyan, I. W. Martin, L. Martinu, B. Maynard, C. S. Menoni, C. Michel, P. G. Murray, C. Osthelder, S. Penn, L. Pinard, K. Prasai, S. Reid, R. Robie, S. Rowan, B. Sassolas, F. Schiettekatte, R. Shink, S. Tait, J. Teillon, G. Vajente, M. Ward, and L. Yang, "Exploration of co-sputtered Ta_2O_5–ZrO_2 thin films for gravitational-wave detectors," Class. Quantum Gravity. **38**(19), 195021 (2021). DOI: https://doi.org/10.1088/1361-6382/ac1b06

[16].   J. Wen, M. Zhu, Y. Chai, T. Liu, J. Shi, W. Du, and J. Shao, "Optical and femtosecond laser-induced damage-related properties of Ta_2O_5-based oxide mixtures," J. Alloy. Compd. **957**, 170352 (2023). DOI: https://doi.org/10.1016/j.jallcom.2023.170352

[17].   G. M. Harry, M. R. Abernathy, A. E. Becerra-Toledo, H. Armandula, E. Black, K. Dooley, M. Eichenfield, C. Nwabugwu, A. Villar, D. R. M. Crooks, G. Cagnoli, J. Hough, C. R. How, I. MacLaren, P. Murray, S. Reid, S. Rowan, P. H. Sneddon, M. M. Fejer, R. Route, S. D. Penn, P. Ganau, J. M. Mackowski, C. Michel, L. and Pinard, A. Remillieux, "Titania-doped tantala/silica coatings for gravitational-wave detection," Class. Quantum Gravity. **24**(2), 405-415 (2007). DOI: https://doi.org/10.1088/0264-9381/24/2/008.

[18].   M. Jacoby, "Thin film helps detect gravitational waves," Science. **3**(2), 92-94 (2017). DOI: https://doi.org/10.1021/acscentsci.7b00049

[19].   M. Molina-Ruiz, K. Shukla, A. Ananyeva, G. Vajente, M. R. Abernathy, T. H. Metcalf, X. Liu, A. Markosyan, R. Bassiri, M. M. Fejer, M. Fazio, L. Yang, C. S. Menoni, F. Hellman, "Low mechanical loss and high refractive index in amorphous Ta_2O_5 films grown by magnetron sputtering," Phys. Rev. Mater. **8**(3), 035603 (2024). DOI: https://doi.org/10.1103/physrevmaterials.8.035603

[20].   R. Henking, D. Ristau, F. V. Alvensleben, and H. Welling, "Optical characteristics and damage thresholds of low loss mirrors," Laser-Induced Damage in Optical Materials: 1994. **27**(1), 281-292 (1995). DOI: https://doi.org/10.1117/12.213744

[21].   J. Zhang, F. Wang, S. Fang, H. Jiao, X. Cheng, Z. Wang, "Scattering and mechanical loss of ultra-low loss laser coatings," Optics and Precision Engineering. **30**(21), 2655-2677 (2022). DOI: https://doi.org/10.37188/ope.20223021.2655

[22].   S. Deng, G. Li, F. Wang, Q. Lv, L. Sun, and Y. Jin, "Study on the Properties of 1319 nm Ultra-High Reflector Deposited by Electron Beam Evaporation Assisted by an Energetic RF Ion Source," Coatings. **8**(2), 72 (2018). DOI: https://doi.org/10.3390/coatings8020074

[23].   L. Kochanneck, J. Rönn, A. Tewes, G. A. Hoffmann, S. Virtanen, P. Maydannik, S. Sneck, A. Wienke, and D. Ristau, "Enabling rotary atomic layer deposition for optical applications," Appl. Optics. **62**(12), 3112-3117 (2023). DOI: https://doi.org/10.1364/ao.477448

[24].   I. A. Alhomoudi, and G. Newaz, "Residual stresses and Raman shift relation in anatase TiO_2 thin film," Thin Solid Films. **517**(15), 4382-4378 (2009). DOI: https://doi.org/10.1016/j.tsf.2009.02.141

[25].   M. Bergler, K. Cvecek, F. Werr, M. Brehl, D. De Ligny, and M. Schmidt, "Cooling rate calibration and mapping of ultra-short pulsed laser modifications in fused silica by Raman and Brillouin spectroscopy," Int. J. Extreme Manuf. **2**(3), 035001 (2020). DOI: https://doi.org/10.1088/2631-7990/ab9583

[26].   S. Boukrouh, R. Bensaha, S. Bourgeois, E. Finot, M. C. and Marco de Lucas, "Reactive direct current magnetron sputtered TiO_2 thin films with amorphous to crystalline structures," Thin Solid Films. **516**(18), 6353-6358 (2018). DOI: https://doi.org/10.1016/j.tsf.2007.12.150

[27].   C. Joseph, P. Bourson, and M. D. Fontana, "Amorphous to crystalline transformation in Ta_2O_5 studied by Raman spectroscopy," J. Raman Spectrosc. **43**(8), 1146-1150 (2012). DOI: https://doi.org/10.1002/jrs.3142

[28].   H. Chen, G. Feng, W. Fan, J. Han, Y. Li, and Q. Lai, "Laser plasma-induced damage characteristics of Ta_2O_5 films," Opt. Mater. Express. **9**(7), 3132-3145 (2019). DOI: https://doi.org/10.1364/ome.9.003132

[29].   J. F. Meng, B. K. Rai, R. S. Katiyar, and A. S. Bhalla, "Raman investigation on $(Ta_2O_5)_{1-x}(TiO_2)_x$ system at different temperatures and pressures," J. Phys. Chem. Solids. **58**(10), 1503-1506 (1997). DOI: https://doi.org/10.1016/s0022-3697(97)00180-7

[30].   S. Roorda, W. C. Sinke, J. M. Poate, D. C. Jacobson, and P. Fuoss, "Structural relaxation and defect annihilation in pure amorphous silicon," Physical Review B Condensed Matter. **44**(8), 3702 (1991). DOI: https://doi.org/10.1103/physrevb.44.3702

[31].   R. Simpson, R. G. White, J. F. Watts, M. A. Baker, "XPS investigation of monatomic and cluster argon ion sputtering of tantalum pentoxide," Appl. Surf. Sci. **405**, 79-87 (2017). DOI:

https://doi.org/10.1016/j.apsusc.2017.02.006

[32]. D. K. Aswal, K. P. Muthe, S. Tawde, S. Chodhury, and J. V. Yakhmi, "XPS and AFM investigations of annealing induced surface modifications of MgO single crystals," J. Cryst. Growth. **236**(4), 661-666 (2002). DOI: https://doi.org/10.1016/s0022-0248(02)00852-7

[33]. A. N. Banerjee, N. Hamnabard, and S. W. Joo, "A comparative study of the effect of Pd-doping on the structural, optical, and photocatalytic properties of sol–gel derived anatase TiO_2 nanoparticles," Ceram. Int. **42**(10), 12010-12026 (2016). DOI: https://doi.org/10.1016/j.ceramint.2016.04.128

[34]. E. Ramos-Moore, P. Ferrari, D. E. Diaz-Droguett, D. Lederman, and J. T. Evans, "Raman and X-ray photoelectron spectroscopy study of ferroelectric switching in $Pb(Nb,Zr,Ti)O_3$ thin films," J. Appl. Phys. **111**(1), 014108 (2012). DOI: https://doi.org/10.1063/1.3675479

[35]. V. Pazhanivelu, A. Paul Blessington Selvadurai, R. Murugaraj, I. Panneer Muthuselvam, and F. C. Chou, "Influence of Co ions doping in structural, vibrational, optical and magnetic properties of ZnO nanoparticles," J. Mater. Sci.-Mater. Electron. **27**(8), 8580-8589 (2016). DOI: https://doi.org/10.1007/s10854-016-4876-8

[36]. E. S. Andres, M. Toledano-Luque, A. D. Prado, M. A. Navacerrada, I. Martil, G. Gonzalez-Diaz, W. Bohne, J. Rohrich, and E. Strub, "Physical properties of high pressure reactively sputtered TiO_2," J. Vac. Sci. Technol. A. **23**(6), 1523-1530 (2005). DOI: https://doi.org/10.1116/1.2056554

[37]. T. Damart, E. Coillet, A. Tanguy, and D. Rodney, "Numerical study of the structural and vibrational properties of amorphous Ta_2O_5 and TiO_2-doped Ta_2O_5," J. Appl. Phys. **119**(17), 175106 (2016). DOI: https://doi.org/10.1063/1.4948665

[38]. R. Bassiri, F. Liou, M. R. Abernathy, A. C. Lin, N. Kim, A. Mehta, B. Shyam, R. L. Byer, E. K. Gustafson, M. Hart, I. MacLaren, I. W. Martin, R. K. Route, S. Rowan, J. F. Stebbins, and M. M. Fejer, "Order within disorder: The atomic structure of ion-beam sputtered amorphous tantala (a-Ta_2O_5)," APL Mater. **3**(3), 158-161 (2015). DOI: https://doi.org/10.1063/1.4913586

[39].   J. H. Hur, "First principles study of the strain effect on band gap of λ phase Ta$_2$O$_5$," Comput. Mater. Sci. **164**, 17-21 (2019). DOI: https://doi.org/10.1016/j.commatsci.2019.03.044

[40].   Z. Zhou, M. Li, and L. Guo, "A first-principles theoretical simulation on the electronic structures and optical absorption properties for O vacancy and Ni impurity in TiO$_2$ photocatalysts," J. Phys. Chem. Solids. **71**(12), 1707-1712 (2010). DOI: https://doi.org/10.1016/j.jpcs.2010.08.021

[41].   F. Xia, Z. Shao, Y. He, R. Wang, X. Wu, T. Jiang, S. Duhm, J. Zhao, S. T. Lee, and J. Jie, "Surface Charge Transfer Doping via Transition Metal Oxides for Efficient p-Type Doping of II-VI Nanostructures," ACS Nano. **10**(11), 10283-10293 (2016). DOI: https://doi.org/10.1021/acsnano.6b05884

[42].   L. Ashraf, S. Waseem, M. T. Qureshi, G. Yunus, L. Aamir, F. Ullah, and M. Saleem, "Structural, electronic, thermoelectric, and optical investigations on Cr substituted Ta$_2$O$_5$," Opt. Mater. **148**, 114901 (2024). DOI: https://doi.org/10.1016/j.optmat.2024.114901

[43].   T. Galy, M. Marszewski, S. King, Y. Feng, Y. Yan, and S. H. Tolbert, "Comparing methods for measuring thickness, refractive index, and porosity of mesoporous thin films," Microporous Mesoporous Mat. **291**, 109677 (2020). DOI: https://doi.org/10.1016/j.micromeso.2019.109677

[44].   C. Mühlig, S. Kufert, S. Bublitz, and U. Speck, "Laser induced deflection technique for absolute thin film absorption measurement: optimized concepts and experimental results," Appl. Optics. **50**(9), 449-456 (2011). DOI: https://doi.org/10.1364/AO.50.00C449

[45].   V. Jain, M. C. Biesinger, and M. R. Linford, The Gaussian-Lorentzian Sum, "Product, and Convolution (Voigt) functions in the context of peak fitting X-ray photoelectron spectroscopy (XPS) narrow scans," Appl. Surf. Sci. **447**, 548-553 (2018). DOI: https://doi.org/10.1016/j.apsusc.2018.03.190

[46].   G. Kresse, and J. Furthmüller, "Efficiency of ab-initio total energy calculations for metals and semiconductors using a plane-wave basis set," Comput. Mater. Sci. **6**(1), 15-50 (1996). DOI:

https://doi.org/10.1016/0927-0256(96)00008-0

[47].   J. P. Perdew, K. Burke, and M. Ernzerhof, "Generalized gradient approximation made simple," Phys. Rev. Lett. **77**(18), 3865-3868 (1998). DOI: https://doi.org/10.1103/physrevlett.77.3865

[48].   S. H. Lee, J. Kim, S. J. Kim, S. Kim, and G. S. Park, "Hidden Structural Order in Orthorhombic Ta_2O_5," Phys. Rev. Lett. **110**(23), 235502 (2013). DOI: https://doi.org/10.1103/physrevlett.110.235502

[49].   C. S. Pedersen, J. H. Chang, Y. Li, N. Pryds, and J. M. Garcia Lastra, "Phase separation in amorphous tantalum oxide from first principles," APL Mater. **8**(7), 071108 (2020). DOI: https://doi.org/10.1063/5.0011390

[50].   R. Bassiri, K. B. Borisenko, D. J. H. Cockayne, J. Hough, I. MacLaren, and S. Rowan, "Probing the atomic structure of amorphous Ta_2O_5 coatings," Appl. Phys. Lett. **98**(3), 031904 (2011). DOI: https://doi.org/10.1063/1.3535982

[51].   J. P. Perdew, A. Ruzsinszky, G. I. Csonka, O. A. Vydrov, G. E. Scuseria, L. A. Constantin, X. Zhou, and K. Burke, "Restoring the Density-Gradient Expansion for Exchange in Solids and Surfaces," Phys. Rev. Lett. **100**(13), 136406 (2008). DOI: https://doi.org/10.1103/physrevlett.100.136406

[52].   J. Heyd, G. E. Scuseria, and M. Ernzerhof, "Hybrid functionals based on a screened Coulomb potential," J. Chem. Phys. **118**(18), 8207-8215 (2003). DOI: https://doi.org/10.1063/1.1564060

[53].   A. Lawal, A. Shaari, R. Ahmed, and N. Jarkoni, "Sb_2Te_3 crystal a potential absorber material for broadband photodetector: A first-principles study," Results Phys. **7**, 2302-2310 (2017). DOI: https://doi.org/10.1016/j.rinp.2017.06.040

[54].   M. Arbi, N. Benramdane, Z. Kebbab, R. Miloua, F. Chiker, and R. Khenata, "First principles calculations of structural, electronic and optical properties of zinc aluminum oxide," Mater. Sci. Semicond. Process. **15**(3), 301-307 (2012). DOI: https://doi.org/10.1016/j.mssp.2012.03.010